Governing Failure Mechanisms of Simplified Three-way Dendritic Branch under Compressive Load

Asghar Aryanfar *†‡, Mounir El Skafi†, Jaime Marian§

† *American University of Beirut, Riad El-Solh, Lebanon 1107 2020*
‡ *Bahçeşehir University, 4 Çırağan Cad, Beşiktaş, Istanbul, Turkey 34349*
§ *University of California, 400 Westwood Plaza, Los Angeles, CA 90095*

©Under the production in Mechanics of Materials ©

Abstract

The growing dendrites during the charging of the battery can pierce into the polymer electrolyte and short-circuit the cell. A dendritic microstructure is a branched medium, consisting of numerous three-way intersections and when subjected to the piercing pressure the corresponding forces propagate throughout the dendrite body. In this paper, we explore the effect of such force propagation versus the geometry of a three-way intersection leading to the failure of a dendritic branch and we have analyzed the dominant failure mechanism in the branch. Particularly we address the mechanics of the intersection versus the respective inclinations of the branches and their normalized length. Generalizing this method into larger clusters of dendritic trees helps to identify the dominant failure mechanism and devise methods to prevent it.

Keywords: Dendritic Structure, Failure Mechanism, Force Propagation, Branch Geometry, Dimensionless Analysis.

1 Introduction

The increasing demand on long-life portable electronics, renewable energy harvesting facilities, computationally powerful and portable computers, as well as the rapidly developing electric vehicles market demands the instigation of energy storage devices with high capacity and efficiency [1, 2, 3]. The conception and development of novel technologies in energy storage devices is falling short behind the expeditious growth in energy consuming lifestyles [4, 5], but the recent advances in rechargeable battery

*Corresponding author; email: aryanfar@caltech.edu

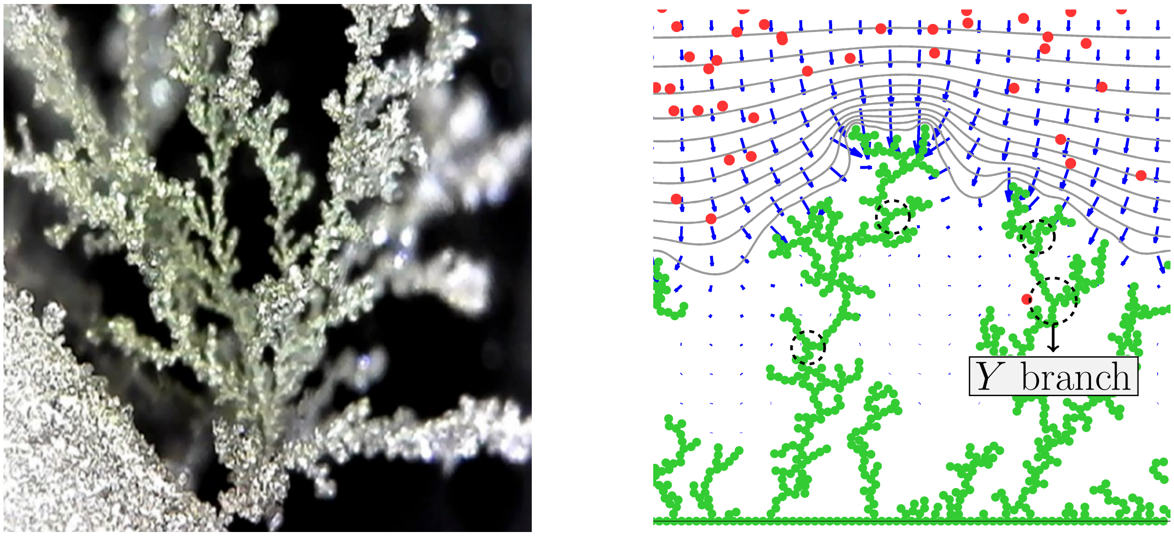

(a) Magnesium dendrites [10]. (b) Dendritic branching [?].

Figure 1: The grown dendritic structures: (a) experimental observation (b) branching sample in the coarse grained model (Green: dendrite, red: free ions, blue: electric field, gray: iso-potential contours) .

technologies produced promising venues for reliable and clean sources for electrical energy and efficient power management [6, 7]. Metallic anodes such as Na [8, 9], Mg [10, 11], Zn [12, 13], and most importantly Li [14, 15, 16, 17], which possesses the highest electropositivity and lowest mass density among these metals, comprise suitable candidates for high energy applications.

The growth and stochastic branching of dendritic structures at the anode during charging occupy large volumes and possess significant surface-to-volume ratios [15] which allows the unstable extension for reaching the counter-electrode and short-circuit the cell [18, 19]. Additionally, the microstructures could detach from the thinner branches throughout charge-discharge cycles, forming isolated crystals which are thermally unstable and lead to capacity fade [20, 21, 22].

Various factors have previously been explored on the formation of the dendritic structures, including temperature [23, 24, 25], directing internal structures [26, 27], utilizing smaller-scale pressure [28], charging method [29, 30, 31], role of particle size on local current density [32], role of solid electrolyte [33], surface perturbations [34, 35], the chemical composition of the electrolyte [36, 37] and its concentration [38] and mechanical strength of the electrode [39, 40]. The recent advanced characterization methods include NMR [41] and MRI [42]. Needless to mention that the control of the solid electrolyte interphase (SEI) which has recently attracted a lot of attention [43, 44].

The predictive modeling of the dendritic structures had initially concentrated on the role of either the electric field [45] or the ionic diffusion [46, 47, 48, 49], whereas the recent studies have covered both effects [50] in a significantly larger scale of the time and space, beyond the double layer region [51]. More recent frameworks include the phase field modeling [52, 53, 54] and use of Tafel kinetics [55].

The tendency of the ionic movement is either moving from higher-to-lower concentrated regions (i.e. diffusion) or from higher-to-lower electric potential (i.e. electromigration). Regarding the dendritic

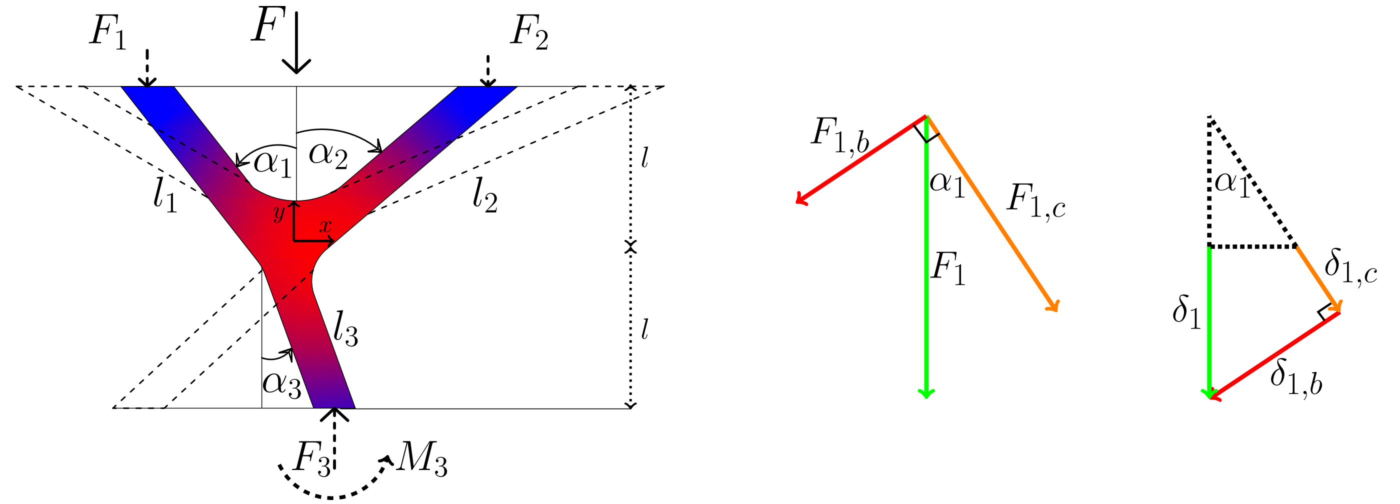

(a) Parametrization of the three-way branch with labelling the involved variables.

(b) The force (left) and deflection (right) decomposition for the branch 1 (left).

Figure 2: The schematics of a three-way branching (a) Y intersection with parametrization (b) Forces and deflections illustration in the left branch.

growth, the former is favorable and the latter is unfavorable, therefore the formation of the dendritic interface is the result of the competition between the two effects.

While the research on dendrites has been difficult due to their amorphous nature and stochastic evolution, the design/selection criterion requires the mechanical compatibility of the evolving dendrites from electrode and the polymer electrolyte. Hence, there is an extensive need for computing the internal forces in the dendritic microstructures for designing the suppression electrolytic separators. This demands computing the mechanics of dendrites for anticipating the onset of piercing into the electrolytic membrane. In this regard, although the branched microstructures extend to continuum scale $\sim \mu m$, they pertain high porosity. Hence, there is not a known experimental investigation of the individual branches and the contemporary images solely visualize their holistic morphology [56, 10, **?**].

In this paper, we develop a multi-mechanism failure criteria for a single three-way dendritic branch, under the compressive load. We analyze the role of the geometrical parameters such as branch orientation, span, and slender-ness ratio as well as the force transmission coefficient and we explain their relationship with the earliest failure mechanism using both analytical expressions and numerical simulations. The obtained characteristic charts could be useful for addressing the mechanical resilience versus the structural complexity, in addition to material per se.

2 Methodology

The dendritic branches in the rechargeable batteries typically grow stochastically, leading to dis-organized trees (Figure 1a) where the material used and operational parameters determine their ultimate morphology.

A single three-way dendritic intersection is represented in the Figure 2a, and the variables are the shown branch angles $\{\alpha_1, \alpha_2, \alpha_3\}$. Since the centered $x-y$ coordinate system has an identical vertical distance l from the top/bottom ends, we have:

$$l_1 \cdot \cos\alpha_1 = l_2 \cdot \cos\alpha_2 = l_3 \cos\alpha_3 = l \tag{1}$$

where the branch lengths $\{l_1, l_2, l_3\}$ will follow as variables. Additionally the imposed force F gets divided to the individual forces F_1 and F_2:

$$F_1 + F_2 = F \tag{2}$$

There are different modes of deflection, based on the magnitude, direction and location of the applied force. Herein, we consider the vertical force F, leading to the identical vertical deflection $\delta_1 = \delta_2$ in both branches. The decompositions of force and displacements are shown in the Figure 2b for the first branch. Hence for the given top branch i, the transmitted forces F_i with the inclination angle α_i causes respective compressive deflection $\delta_{i,c}$ due to compression component $F_{i,c} = F_i \cos\alpha_i$ along axial directions as well as the bending deflection $\delta_{i,b}$ due to bending component $F_{i,b} = F_i \sin\alpha_i$ perpendicular to the branch i, that can be obtained as [57]:

$$\begin{cases} \delta_{i,c} = \dfrac{F_i l_i}{AE} \cos\alpha_i \\ \delta_{i,b} = \dfrac{F_i l_i^3}{3EI} \sin\alpha_i \end{cases} \tag{3}$$

where F_i is the vertical force on either branch and l_i , $A = \frac{\pi}{4}d^2$, $I = \frac{\pi}{64}d^4$ and E are the length, cross sectional area, the second moment of inertia and the elastic modulus of the branch. Consequently, from Figure 2b the total vertical displacement δ is obtained via superposition as:

$$\delta_i = \delta_{i,c} \cos\alpha_i + \delta_{i,b} \sin\alpha_i \tag{4}$$

Coupling Equations 4 and 3 relates the forces F_i in each branch to their respective total vertical displacements δ_i. Hence, the equal deflection criterion ($\delta_1 = \delta_2$) leads to:

$$\frac{F_1 l_1}{AE}\cos^2\alpha_1 + \frac{F_1 l_1^3}{3EI}\sin^2\alpha_1 = \frac{F_2 l_2}{AE}\cos^2\alpha_2 + \frac{F_2 l_2^3}{3EI}\sin^2\alpha_2 \tag{5}$$

Solving the coupled equation of 2 and 5 leads to the individual branch forces $F_i = f_i F$, where the fraction f_i is the force transmission coefficient for the respective branch i, simplified as:

$$f_i = 1 - \frac{\eta_i}{\sum \eta_i} \tag{6}$$

where the coefficient η_i is expressed as:

$$\eta_i = \cos\alpha_i + \frac{16}{3\pi}\hat{l}_i^2 \sin\alpha_i \tan\alpha_i \tag{7}$$

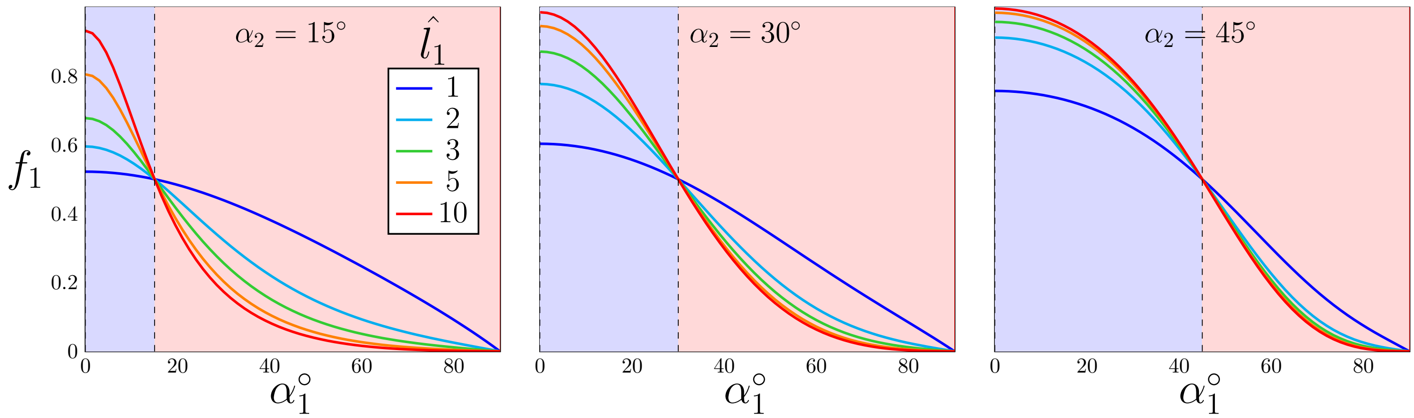

(a) $\alpha_2 = 15°$ (b) $\alpha_2 = 30°$ (c) $\alpha_2 = 45°$

Figure 3: Variation of force transmission coefficient f_1 versus the branch angle α_1 for different values of the other branch angle $\alpha_2 = \{15°, 30°, 45°\}$. The blue zone illustrates the dominance of the branch 1 ($F_1 > F_2$), while the red zone shows the opposite ($F_1 < F_2$).

here $\hat{l}_i := \dfrac{l_i}{d}$ is the non-dimensionalized branch length. The force transmission coefficient f_i is extensively explored versus the respective branch angle α_i in the Figure 3 as well as the branch length $\hat{l}_1 = \{1, 2, 3, 5, 10\}$ (each figure) and the angles of the other branch $\alpha_2 = \{15°, 30°, 45°\}$.

The failure of the three-way dendritic branch could be due to yielding (i.e. compression + bending) or buckling. Region-wise, we categorize the failure as below:

2.1 Top Failure:

I. Yielding (Y): The compressive stress σ_i in the branch i is the cooperative effect of bending ($F_{i,b}$) and compression ($F_{i,c}$) forces, and it's maximum occurs at the intersection end which has longest arm for bending, as below:

$$\sigma_i = \frac{F_{i,b} l_i c}{I} + \frac{F_{i,c}}{A} \tag{8}$$

where $c = \dfrac{d}{2}$ is the maximum distance from the neutral axis. Considering Equations 6 and 8 and to prevent failure we require $\sigma_i < \sigma_y$, then the yielding force in the top branch $\hat{F}_{\text{Top},Y}$ in the dimension-less form is obtained as:

$$\hat{F}_{\text{Top},Y} < \frac{1}{f_i} \frac{1}{8\hat{l}_i \sin\alpha_i + \cos\alpha_i} \tag{9}$$

where $\hat{F} = \dfrac{F}{A\sigma_y}$ and $\hat{l}_i = \dfrac{l_i}{d}$. Since the metal's strength is similar in both tension and compression, the interaction of the compressive force $F_{i,c}$ and compressive/tensile moment $F_{i,b} l_i$ in the arm i has been only conservatively considered for their constructive effect (plus sign).

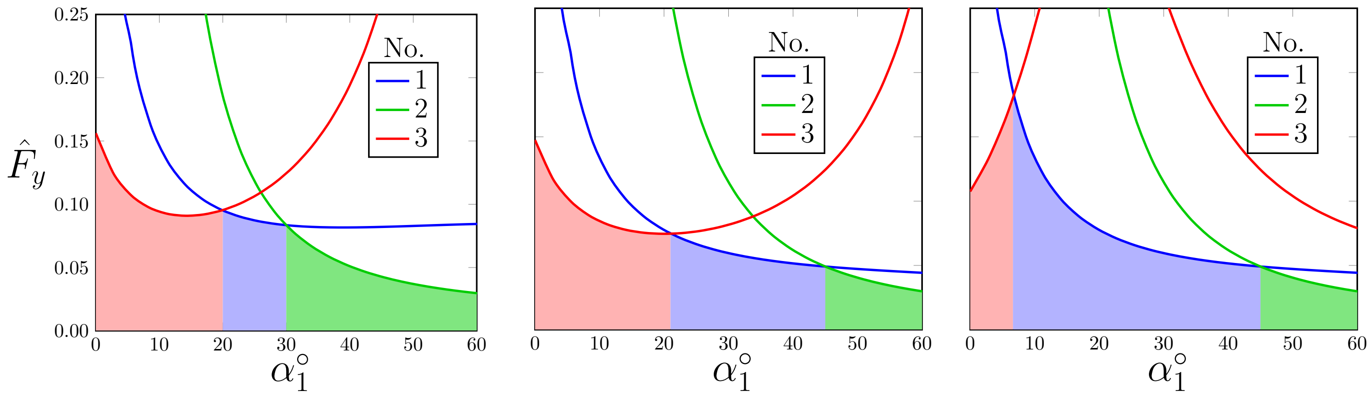

(a) $\alpha_2 = 30°, \alpha_3 = 10°$ (b) $\alpha_2 = 45°, \alpha_3 = 10°$ (c) $\alpha_2 = 45°, \alpha_3 = -10°$

Figure 4: Non-dimensional critical force $\hat{F}$ for yielding failure versus the inclination angle α_1 and $\hat{l} = 5$. The zones of the earliest failure are shaded (branch 1 (right) in blue, and branch 2 (left) in green and branch 3 (bottom) in red).

II. Buckling (B): Additionally, for a top branch i in the Figure 2a with the free top (moving) and the fixed bottom (intersection), the critical axial force $F_{ic,B}$ would be $F_{ic,B} = \frac{1}{4}\frac{\pi^2 EI}{l_i^2}$[58] , and based on the parameters of the Figure 2a ($l_i = \frac{l}{\cos\alpha_i}$, $F_i = f_i F \cos\alpha_i$) the critical load $\hat{F}_{\text{Top},B}$ is obtained as:

$$\hat{F}_{\text{Top},B} = \frac{\cos\alpha_i}{\epsilon_y f_i}\left(\frac{\pi}{8\hat{l}_i}\right)^2 \tag{10}$$

2.2 Bottom Failure:

I. Yielding (Y): The compressive stress experienced in the bottom occurs is the result of the difference of the top moments from the left/right branches as well as the transmitted compression. From the Figure 2a, the direction of α_1, α_2 and α_3 are considered as CCW[1], CW[2] and CCW respectively. The applied force F is decomposed to the axial $F_{3,c}$ and bending $F_{3,b}$ forces with moment M_3, obtained as:

$$F_{3,c} = F\cos\alpha_3\ ,\ \ F_{3,b} = F\sin\alpha_3\ ,\ M_3 = Fl\Delta \tag{11}$$

where, $\Delta = f_1\tan\alpha_1 - f_2\tan\alpha_2 + (f_1 - f_2)\tan\alpha_3$, and the length is $l_3 = \frac{l}{\cos\alpha_3}$. Hence on the applied force should fall in the following range ($\alpha_3 > 0$), in dimension-less form:

$$\hat{F}_{\text{Bot},Y} < \frac{1}{8\hat{l}\Delta + \cos\alpha_3} \tag{12}$$

[1]Counter clock-wise.
[2]Clock-wise.

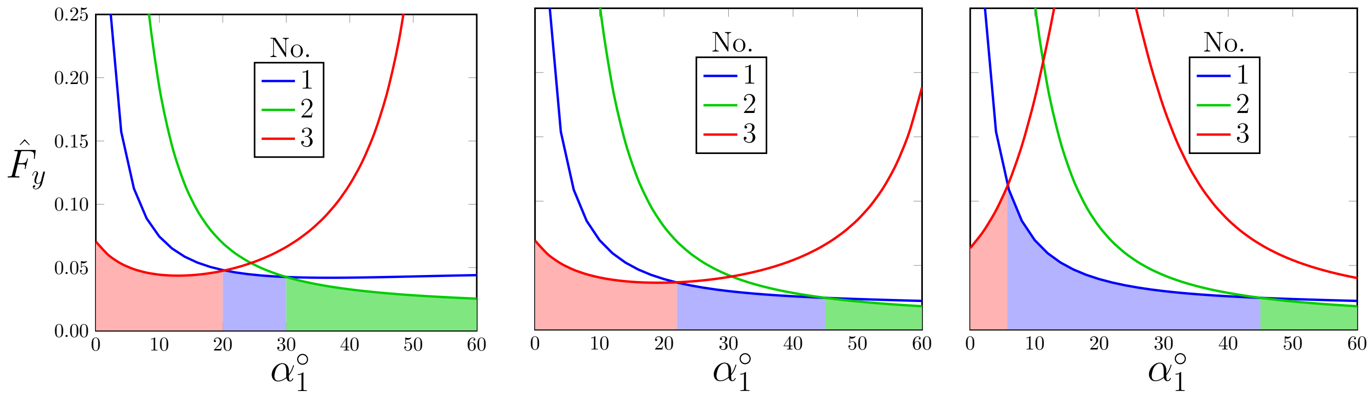

(a) $\alpha_2 = 30°, \alpha_3 = 10$ (b) $\alpha_2 = 45°$, $\alpha_3 = 10$ (c) $\alpha_2 = 45°$, $\alpha_3 = -10°$

Figure 5: Non-dimensional critical force $\hat{F}$ for yielding failure versus the inclination angle α_1 and $\hat{l} = 10$. The zones of the earliest failure are shaded (branch 1 (right) in blue, and branch 2 (left) in green and branch 3 (bottom) in red).

II. Buckling (B):

Figure 7 illustrates the free body diagram for the branch 3 (bottom) as a function of the geometric parameters. The moment equilibrium in the distance x yields:

$$EIy" + (F\cos\alpha_3)\,y = -(F\sin\alpha_3)\,x + M_3$$

which could be solved in terms of the homogenous y_h and particular y_p solutions as:

$$y = A\sin(\lambda x) + B\cos(\lambda x) - (\tan\alpha_3)\,x + \frac{M_3}{F\cos\alpha_3} \tag{13}$$

where $\lambda = \sqrt{\dfrac{F\cos\alpha_3}{EI}}$. Assuming the cantilever boundary condition in the bottom ($y(0) = 0$, $y'(0) = 0$) and the pinned condition in the top ($y(l) = 0$) one arrives as:

$$\sin\alpha_3\,(\lambda l - \sin(\lambda l)) = \frac{M_3}{F}\lambda\,(1 - \cos(\lambda l)) \tag{14}$$

which could be solved numerically for obtaining the critical force F. For a simpler case of vertically standing bottom branch ($\alpha_3 = 0$), the analytical solution would be:

$$y = \Delta l\left(1 - \cos\left(\sqrt{\frac{F}{EI}}x\right)\right)$$

Which in order to yields $y(l) = 0$ one arrives at:

$$F_{3c,cr} = 4\frac{\pi^2 EI}{l_3^2}$$

which, based on the given configuration it translates into:

$$\hat{F}_{\text{Bot},B} = \frac{\cos\alpha_3}{\epsilon_y}\left(\frac{\pi}{2\hat{l}}\right)^2 \tag{15}$$

Additionally, in a typical dendritic branch the slenderness ratio $\frac{l}{\kappa}$ is considerable and hence, compared to yielding due to bending and compression, the buckling is less likely to occur. Nonetheless for the elastic buckling, the lowest slenderness ratio limit is found to be $\left(\frac{l}{\kappa}\right)_{min} = \frac{\pi}{\sqrt{\epsilon_y}}$ [59]. Hence the geometric range for elastic buckling via considering circular cross-section and simplification will be:

$$\hat{l}^2 > \frac{\pi^2}{16\epsilon_y} \tag{16}$$

Considering the typical yield strain of $\approx 0.2\%$ for metals [60], one gets:

$$\hat{l} > 17.56$$

which will be verified for elastic buckling in the next section.

Figures 4 and 5 show the graphs of the critical failure zones caused by the force $\hat{F}$ considering all three branches of the three-way intersection for $\hat{l}_1 = 5$ and $\hat{l}_1 = 10$ respectively. The shaded areas represent the mechanism of the earliest failure where the blue, red, and green regions signify the yielding failure in the branches 1 , 2 (Top) and 3 (Bottom) respectively. In this regard, the failure is defined as the minimum force causing of the aforementioned mechanisms, as below:

$$\hat{F}_{\text{Top}} = \min\left\{\hat{F}_{\text{Top},Y}, \hat{F}_{\text{Top},B}\right\} \;\; , \; \hat{F}_{\text{Bot}} = \min\left\{\hat{F}_{\text{Bot},Y}, \hat{F}_{\text{Bot},B}\right\}$$

Mainly the branch with the smallest angle fails earlier (branch 1 for $\alpha_1 < \alpha_2$ and branch 2 vice versa). However, the bottom part fails first for large-enough values of α_1, where the moment difference between the top branches becomes significant. As well, when $\alpha_1 \to 0$, although both top and bottom are dominantly in compression, the bottom parts bears more force since the top force still gets divided, therefore the bottom failure becomes slightly dominant.

3 Symmetric case ($\alpha_1 = \alpha_2 = \alpha$, $l_1 = l_2 = l_3$)

In this case the angle with vertical axis is α, and the length of the branches is $\hat{l}$ while geometric and mechanical conditions are symmetric. Therefore, the Equation 9 reduces to:

$$\hat{F}_{\text{Top},Y} < \frac{2}{8\hat{l}\tan\alpha + \cos\alpha} \tag{17}$$

As well the bottom yielding force is simplified into $\hat{F} = 1$. The Figure 6 shows the critical failure

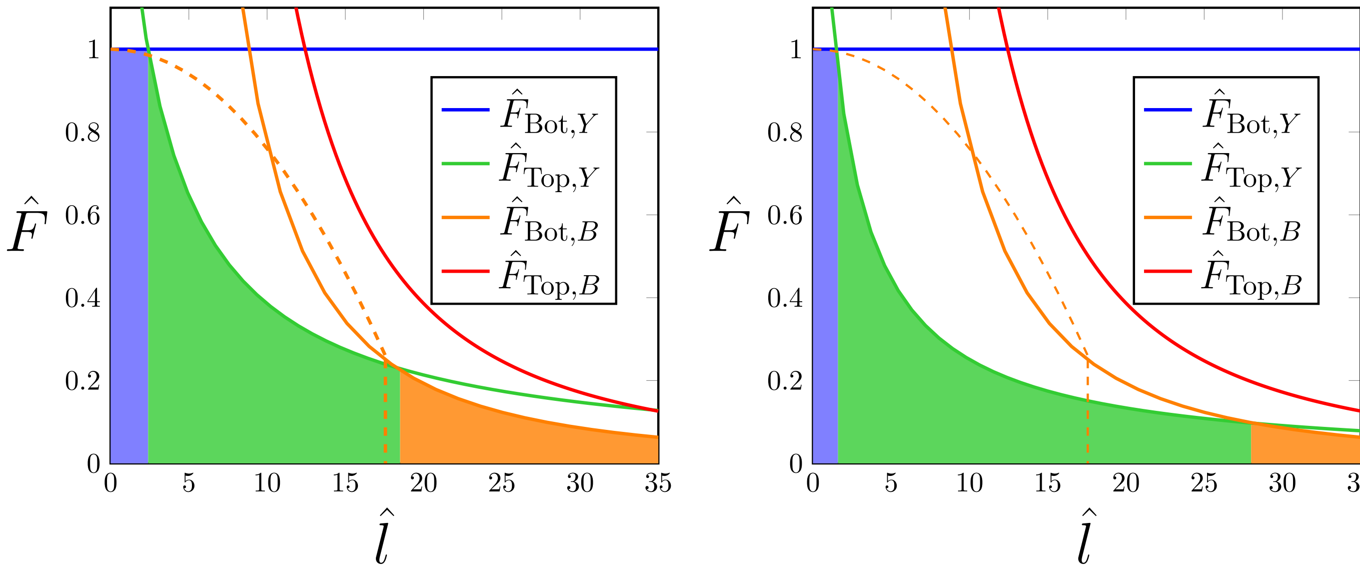

(a) $\alpha = 3°$

(b) $\alpha = 5°$

Figure 6: The critical force $\hat{F}$ in symmetric case ($\alpha_1 = \alpha_2 = \alpha, \hat{l}_1 = \hat{l}_2 = \hat{l}_3$) versus the non dimensional length $\hat{l}$. The figures show regions of the earliest failure, either by yielding in the bottom (blue), yielding in the top (green) buckling of the bottom branch (orange). The dashed line shows the limit of the inelastic buckling.

zones for the symmetric case of $\alpha = \{3°, 5°\}$ against the branch length $\hat{l}$. For a very small $\hat{l}$, the failure occurs in the bottom by yielding which is highlighted in blue. The next region for higher $\hat{l}$, shows the failure by yielding of the top branch (it is indifferent which branch fails due to symmetry). This region is highlighted in green. Increasing further in $\hat{l}$, the failure mechanism becomes buckling of the bottom branch highlighted in orange. However, since the top force gets divided, it is unlikely that the structure fails by buckling of the top branches (red curve). As well, the explored configurations in these graphs, which is attained from the Equation 16 falls beyond the inelastic limit (dashed curve in the Figures 6a and 6b) and hence the failure takes place within the elastic range.

4 Numerical Simulations

We have performed numerical simulations via ABAQUS on the intersection of three branches with the concerned geometries. The simulation intersection was established via joining the beams of circular cross-section and assigning the identical values in their translation and rotation values. The top two branches were assigned free displacements in their top, while the the bottom branch was assigned cantilever condition (i.e. no translation/rotation) in the bottom end. The meshing was performed via default wire elements in two dimensions. Subsequently, the equal vertical displacements were imposed to the top branches and the simulation was run for the statics case in one single step. Care was taken so the maximum stress value does not exceed the yield strength of the assigned material ($\sigma < \sigma_y$). The resulting figures for the assigned geometries are shown in the Figure 8, for analogy with the attained analytical trend, which, are in agreement as illustrated in 3 configurations. Due to non-dimensional

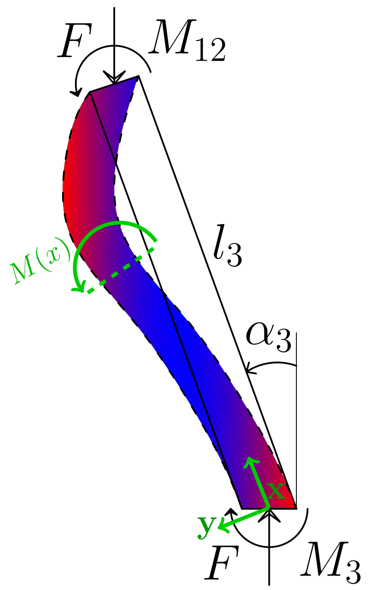

Figure 7: The free body diagram for the buckling of the branch 3, which occurs for large-enough branch length $\hat{l}$. The color distribution is proportional to the criticality of the internal stresses.

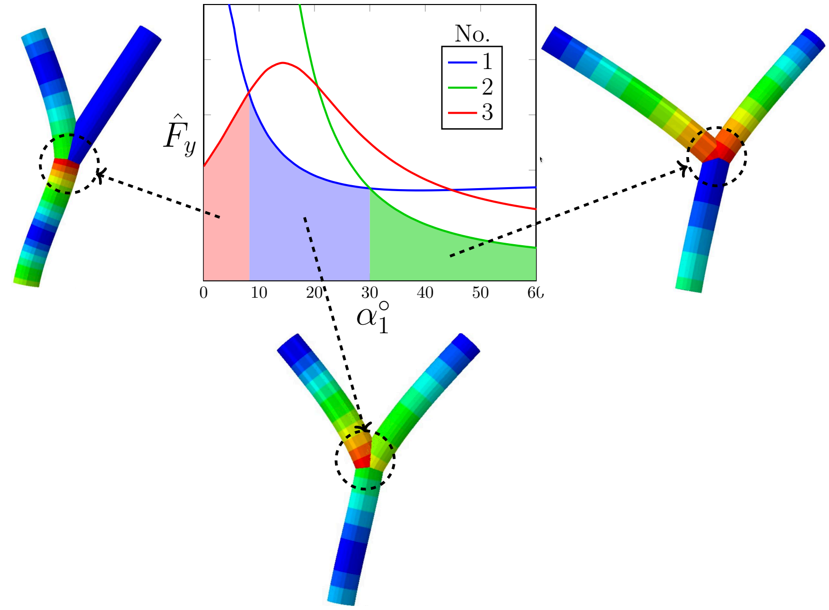

Figure 8: Analogy of the analytically-attained critical force with the simulations. In each geometric configuration the failed branch is identified with the same branch of highest stress value $\alpha_2 = 30°, \alpha_3 = -10°, \hat{l} = 5$. Since $\alpha_3 < 0$, the yieldig of branch 3 (bottom) occurs toward the top end (center).

nature of the graphs, the trend is true for any given arbitrary material and the location of the maximum stress will not change, as long as the entire medium remains in elastic (i.e. linear) zone.

5 Results & Discussions

In a broad view, the failure in each branch of the three-way intersection depends on the combination of bending+compression (Y), and bucking (B) stresses, which are separately functions of the inclination angle α_i, and consequently branch length l_i and the force transmission coefficients f_i. From the Equation 3, one gets the following:

$$\begin{cases} \delta_{i,c} \sim f_i l_i \cos \alpha_i \\ \delta_{i,b} \sim f_i l_i^3 \sin \alpha_i \end{cases}$$

Comparing the parameters f_i, l_i and α_i, for vertical-enough branch the angle dependency α_i is the most dominant ($\delta_{i,c} > \delta_{i,b}$). However for large-enough values of branch orientation α_i, the length dependency l_i becomes higher and the bending deflection takes over ($\delta_{i,b} > \delta_{i.c}$).

From the Figure 3 it is obvious that the most vertical branch always takes the highest portion of the applied force F ($f_i \uparrow \sim \alpha_i \downarrow$). As well, the transition of the branch with the higher force fraction occurs when the geometry approaches the symmetric case ($\alpha_1 \to \alpha_2$) leading to $f_1 \approx f_2 \to 0.5$. Therefore increasing the angle for the second branch α_2 makes the transition point of the branch with dominant force move to higher values. As well due to transition of the dominancy, the rate of the force exchange $\partial f_1/\partial\alpha_1$ is mostly highest in the proximity of symmetricity. Finally, this rate $\partial f_1/\partial\alpha_1$ is larger for the longer branch length l since the bending deflection has the highest sensitivity to the branch length.

Before the transition (i.e. $\alpha_1 < \alpha_2$) the branch l_2 is larger, and thus the dominant modes of deflection is compression δ_c for left branch and bending δ_b for the right branch. From the Equation 3 obviously $\delta_b \propto l^3$ and $\delta_c \propto l$. Thus, increasing α_1 causes bending deflection δ_b to increase more significantly both in terms of angle α_1 and length l_1. After the transition point ($\alpha_1 > \alpha_2$) the dominant modes of deflections are exchanged. While the left branch bears larger bending deflection δ_b and becomes susceptible to failure as α_1 grows, the right branch will encounter the larger force fraction f_2. To summarize:

$$\alpha_i \uparrow \;\sim\; f_i \downarrow \;\sim\; l_i \uparrow$$

and therefore the trends of compressive $\delta_{i,c}$ and bending $\delta_{i,b}$ deflections are the result of their cumulative effect.

Comparing the the trend for the top branches 1 and 2 in the Figure 3 with the Figures 4 and 5 one notices the correlation between force fraction f_i and the respective failure region, where the branch of the largest force fraction f_i fails the earliest. Additionally, the sensitivity to the branch length $\hat{l}$ is obvious by contraction of the failures zones in the 5 ($\hat{l}_1 = 10$) with respect to the Figure 4 ($\hat{l}_1 = 5$). As well, the the contribution of buckling forces in failure is absent in these figures and becomes more pronounced for larger branch length values (i.e. $F_{B,i} \propto l_i^{-2}$). Nonetheless, the order of the yielding for all explored configurations versus the branch orientation α_1 is bottom yielding (branch 3), top left yielding (branch 1) and top right yielding (branch 2).

Analyzing the symmetric case is relatively simpler in the Figure 6, where the bottom branch becomes only critical for small values of $\alpha_1 \approx \alpha_2$ which leads to smaller values branch lengths $\hat{l}_1 \approx \hat{l}_2$, particularly due to neutralizing of the imposed moments from the top branches (i.e. $\left| f_1 \hat{l}_1 sin\alpha_1 - f_2 \hat{l}_2 sin\alpha_2 \right| \approx 0$). However, the larger values of $\hat{l}_i$ and angle α_i triggers the bending failure for the top branches. (i.e. $\hat{F}_{\mathrm{Top}_{1,2},Y} < \hat{F}_{\mathrm{Bot},Y} \approx 1$). This can be shown from Equation 17 where the yielding limit shrink linearly with extra length $\hat{l}$. On the other hand, this function is dynamically variant versus α, and to find the minimum value from the Equation 9 we find α for which:

$$\frac{\partial \hat{F}_{\mathrm{Top},Y}}{\partial \alpha} = \frac{2\left(\sin\alpha\cos^2\alpha - 8\hat{l}\right)}{\left(8\hat{l}\sin\alpha + \cos^2\alpha\right)^2} < 0$$

which is due to larger typical value $\hat{l}$. Thus, the maximum force $\hat{F}_{\mathrm{Top},Y}$ will reduce versus the angle α monotonously, which is mainly due to bending effect becoming more critical ($\hat{l}\uparrow$).

Additional increasing branch length makes the buckling threshold in the bottom branch to shrink with higher rate that eventually surpasses the yielding limit in the top branches. Comparing the two terms in the Equations 15 and 9, such length limit is found as:

$$\hat{l}_{Y\to B} = \frac{\pi^2}{2\varepsilon_y}\left(\tan\alpha + \sqrt{\tan^2\alpha + \frac{\varepsilon_y}{2\pi^2}\cos\alpha}\right)$$

which shows the direct correlation between the transition length $\hat{l}_{Y\to B}$ and the branch angle α. In fact, the smaller branch inclination α, the transition from yielding Y to the bucking B occurs earlier and in the limit one gets:

$$\hat{l}^{\min}_{Y\to B} = \frac{\pi}{2\sqrt{2\varepsilon_y}} \approx 24.8 \tag{18}$$

which is obtained via the assumption of $\epsilon_y = 0.2\%$ and resonates very well with the transient regime in the Figures 6a and 6b. As well, Equation 18 shows that for ductile materials that have higher yield strain ε_y causes the material endure larger deflection in bending. Thus the buckling becomes more controlling for the failure and the transition length $\hat{l}_{Y\to B}$ from bending failure to buckling failure becomes smaller. Vice versa brittle materials with smaller ε_y are highly sensitive to bending and therefore the failure is controlled more by yielding (compression + bending) failure than the buckling failure. As well, the possibility of buckling is highly sensitivity to the angle α and occurs when the length is considerably high ($l \uparrow$) or the corresponding angle is very small ($\alpha \downarrow$). Therefore, for large enough inclinations, yielding becomes a sole failure mechanism.

It is obvious that the bottom buckling always occurs earlier than the top, since the force in the top branch is the result of decomposition of the imposed force to the fraction of f_i and to the axial direction by means of the the projection Therefore, in the symmetric case $\frac{1}{2}\cos\alpha < 1$, $f_i = \frac{1}{2}$ and:

$$F_1 = F_2 < F_3$$

and hence the buckling in the Figures 6 is always controlled by the bottom branch. Furthermore one could explore the possibility of the moment amplification in the deflected branch, where the imposed and generated moments reduce the threshold for the critical load. For symmetric case, one could set $\alpha_3 = 0$ and the Equation 13 is reduced to:

$$y = \frac{M_3}{F}\left(1 - \cos\left(\sqrt{\frac{F}{EI}}x\right)\right)$$

The most critical position x_c for the moment amplification could be found by setting $y'(x) = 0$, hence getting $x_c = \pi\sqrt{\frac{EI}{F}}$, the magnitude of maximum deflection y_{max} would be obtained as $y_{max} = \frac{2M_3}{F}$. From the Equation 11, on the verge of yielding, one has:

$$\frac{F}{A} + \frac{F.y_{max}.c}{I} + \frac{M_3 c}{I} = \sigma_y$$

which gets simplified to:

$$\hat{F} = \frac{1}{1 + 24\Delta\hat{l}} \tag{19}$$

Comparing with the Equation 12, this is a stricter criterion for the failure. In fact the moment amplification triples the effect of the transmitted moment M_3 to the branch 3, and hence could be controlling when the magnitudes of the transmitted moment M_3 and the branch length $\hat{l}$ are sufficiently large. However, for the symmetric case, $\Delta \to 0$ and hence $\hat{F} \to 1$, which will not be deterministic mechanism for the the trends of the Figures 6a and 6b.

Finally, we should mention that this study is simplistic approach to the failure of a single three-way junction in the local level and additional rotation/translation from the global frame of reference could be deterministic for the failure mode as well as the the criticality of a branch. Hence, further cluster-based generic work is underway in order to include role the entire structure as well as the magnitude/orientation of the propagated force, ending up in the concerned junction, which could be added to the framework by means of superposition in throughout the elastic behavior. In fact, the combination of the failure modes during the plastic behavior would be conditional and non-linear which pertains higher level of complexity and further work is underway for addressing their association during the plastic behavior.

Needless to mention that in the presence of defects, the branches could undergo fracture in the lower regime of the loading. However, since the dendritic branches are usually in sub-grain ($\sim \mu m$) scale, the possibility of formation of imperfections is lower than the larger scales. The scarcity of defects in smaller scale has been attributed as the underlying reason for the higher strength in the lower scales [61, 62].

Additionally, in this study we have considered the piercing force as a major stress source on the three-way dendritic branch. During the initial growth of the dendrites, there are other minor stress sources, such as the surrounding organic compounds and hydrostatic pressure where the net effect could perhaps become tangible in large-enough scales. There are additional the side physical effects, such as presumably the moments in the junction and the interaction of the three-way dendritic branch via external contact with the neighbor branch(es), which is not included. Not to mention that the surrounding fluid (i.e. electrolyte) will have a balanced-out the pressure distribution from the periphery (Pascal's law), which ultimately have neutral net effect.

However, the major part of dendritic growth occurs in the space between the components which is the gap between the electrode and electrolyte. Hence, the external effects are minimized. Nevertheless these factor still remains minimal compared to the piercing forces.

6 Conclusion

In this paper, we developed a geometric framework for the failure of a three-way intersection as the most critical part of a microstructure where the role of the branch length and the corresponding branch orientation with the respective force fraction is analyzed extensively. The failure mechanism due to vertical loading has been explored in terms of three distinct mechanisms of bending, compression and buckling and zones of earliest failure were respectively identified and visualized. In particular, the symmetric junction case was explored further where the buckling effect was investigated by extending the branches length beyond the typical limits. The failure analysis was performed in dimensionless form, making the characterization scale-free.

The deflection based analysis showed that the force is transmitted dominantly into the least inclined branch, and the force transmission coefficient declines as the inclination angle increases. As well, the transition point of controlling force between the top branches occurs at symmetric configuration.

The governing failure mechanism for the three-way junction is yielding due to bending for the largest sensible range of parameters, and buckling becomes relevant for failure only in exceptionally large branch lengths and small inclination angles. In this regard, the moment amplification during the buckling has shown to have significant effect, which could be controlling factor in non-symmetric cases.

The failure analysis in this study is constructive for assessing the mechanical properties of a large-scale dendrite where the realization between the structural configuration and failure mechanism and the respecrice limit allows computing the transmitted force from microstructure to a neighboring polymer electrolyte or other mechanical barriers.

Acknowledgement

The authors would like to thank and recognize financial support for the Research Assistant Mounir El Skafi from the Masri Institute, Award #103919 at American University of Beirut.

List of Symbols

E : Elastic modulus (pa)
l_i : Length of branch i (m)
$\hat{l}_i$: Normalized length of branch i
d : Diameter of branch (m)
α_i : Inclination angle between the vertical axis and branch i (rad)
F: Total force applied (N)
F_i: the total force on the branch i
$F_{i,c}$: Force due to compression in branch i (N)
$F_{i,b}$: Force due to bending in branch i (N)
$F_{Top,Y}$: Yielding force in the top branch (N)
η_i: coefficient for calculating f_i
M_{12} : Moment transmitted to the branch 3 (top) ($N.m$)
M_3 : Moment reaction from the branch 3 (bottom) ($N.m$)
Δ: Coefficient of moment reaction from the branch 3 ([ ])
$F_{Bot,Y}$: Yielding force in the bottom branch(N)
$F_{Top,B}$: Buckling force in top branch (N)
$F_{Bot,B}$: Buckling force in bottom branch (N)
$\hat{F}$: Normalized force applied
I : Areal moment of inertia (m^4)
δ_i: Total deflection in branch i (m)
$\delta_{i,c}$: deflection due to compression in branch i (m)
$\delta_{i,b}$: deflection due to bending in branch i (m)
A: cross-section (m^2)
σ_y : Yield stress (pa)
ϵ_y: Yield strain ([ ])
x: Distance coordinate for branch 3 (m)
y: Deflection coordinate for branch 3 (m)
x_c: location of maximum deflection (m)
y_{max}: the magnitude of the maximum deflection (m)
κ: The radius of gyration (m)

Data Availability

The row data for producing the results in this manuscript are freely available upon request from the corresponding author at aryanfar@caltech.edu.

Conflict of Interest Statement

The authors declare that they have no competing financial interests to influence the work reported in this paper.

References

[1] Srdjan M Lukic, Jian Cao, Ramesh C Bansal, Fernando Rodriguez, and Ali Emadi. Energy storage systems for automotive applications. *IEEE Transactions on industrial electronics*, 55(6):2258–2267, 2008.

[2] Paulo F Ribeiro, Brian K Johnson, Mariesa L Crow, Aysen Arsoy, and Yilu Liu. Energy storage systems for advanced power applications. *Proceedings of the IEEE*, 89(12):1744–1756, 2001.

[3] Hussein Ibrahim, Adrian Ilinca, and Jean Perron. Energy storage systems: Characteristics and comparisons. *Renewable and sustainable energy reviews*, 12(5):1221–1250, 2008.

[4] Peter G Bruce, Laurence J Hardwick, and KM Abraham. Lithium-air and lithium-sulfur batteries. *MRS bulletin*, 36(7):506–512, 2011.

[5] Nick Eyre, Jillian Anable, Christian Brand, Russell Layberry, and Neil Strachan. The way we live from now on: lifestyle and energy consumption. *Energy 2050: Making the Transition to a Secure Low-Carbon Energy System*, pages 258–93, 2010.

[6] Rotem Marom, S Francis Amalraj, Nicole Leifer, David Jacob, and Doron Aurbach. A review of advanced and practical lithium battery materials. *Journal of Materials Chemistry*, 21(27):9938–9954, 2011.

[7] John B Goodenough and Kyu-Sung Park. The li-ion rechargeable battery: a perspective. *Journal of the American Chemical Society*, 135(4):1167–1176, 2013.

[8] Michael D Slater, Donghan Kim, Eungje Lee, and Christopher S Johnson. Sodium-ion batteries. *Adv. Funct. Mater.*, 23(8):947–958, 2013.

[9] Brian L Ellis and Linda F Nazar. Sodium and sodium-ion energy storage batteries. *Current Opinion in Solid State and Materials Science*, 16(4):168–177, 2012.

[10] Rachel Davidson, Ankit Verma, David Santos, Feng Hao, Coleman Fincher, Sisi Xiang, Jonathan Van Buskirk, Kelvin Xie, Matt Pharr, Partha P Mukherjee, et al. Formation of magnesium dendrites during electrodeposition. *ACS Energy Letters*, 4(2):375–376, 2018.

[11] Ivgeni Shterenberg, Michael Salama, Yossi Gofer, Elena Levi, and Doron Aurbach. The challenge of developing rechargeable magnesium batteries. *Mrs Bulletin*, 39(5):453–460, 2014.

[12] Pucheng Pei, Keliang Wang, and Ze Ma. Technologies for extending zinc air batterys cyclelife: A review. *Applied Energy*, 128:315–324, 2014.

[13] Yanguang Li and Hongjie Dai. Recent advances in zinc–air batteries. *Chem. Soc. Rev.*, 43(15):5257–5275, 2014.

[14] Siyuan Li, Jixiang Yang, and Yingying Lu. Lithium metal anode. *Encyclopedia of Inorganic and Bioinorganic Chemistry*, pages 1–21.

[15] W. Xu, J. L. Wang, F. Ding, X. L. Chen, E. Nasybutin, Y. H. Zhang, and J. G. Zhang. Lithium metal anodes for rechargeable batteries. *Energy and Environmental Science*, 7(2):513–537, 2014.

[16] Aruna Zhamu, Guorong Chen, Chenguang Liu, David Neff, Qing Fang, Zhenning Yu, Wei Xiong, Yanbo Wang, Xiqing Wang, and Bor Z Jang. Reviving rechargeable lithium metal batteries: enabling next-generation high-energy and high-power cells. *Energy Environ. Sci.*, 5(2):5701–5707, 2012.

[17] Bruno Scrosati and JÃŒrgen Garche. Lithium batteries: Status, prospects and future. *J. Power Sources*, 195(9):2419–2430, 2010.

[18] Ji-Hyung Han, Miao Wang, Peng Bai, Fikile R Brushett, and Martin Z Bazant. Dendrite suppression by shock electrodeposition in charged porous media. *Scientific reports*, 6(1):1–12, 2016.

[19] Wei Liu, Pengcheng Liu, and David Mitlin. Tutorial review on structure–dendrite growth relations in metal battery anode supports. *Chemical Society Reviews*, 49(20):7284–7300, 2020.

[20] Deepti Tewari, Sobana P Rangarajan, Perla B Balbuena, Yevgen Barsukov, and Partha P Mukherjee. Mesoscale anatomy of dead lithium formation. *The Journal of Physical Chemistry C*, 2020.

[21] Yi-Chen Hsieh, Marco Leißing, Sascha Nowak, Bing-Joe Hwang, Martin Winter, and Gunther Brunklaus. Quantification of dead lithium via in situ nuclear magnetic resonance spectroscopy. *Cell Reports Physical Science*, 1(8):100139, 2020.

[22] Kuan-Hung Chen, Kevin N Wood, Eric Kazyak, William S LePage, Andrew L Davis, Adrian J Sanchez, and Neil P Dasgupta. Dead lithium: mass transport effects on voltage, capacity, and failure of lithium metal anodes. *Journal of Materials Chemistry A*, 5(23):11671–11681, 2017.

[23] Asghar Aryanfar, Tao Cheng, Agustin J Colussi, Boris V Merinov, William A Goddard III, and Michael R Hoffmann. Annealing kinetics of electrodeposited lithium dendrites. *The Journal of chemical physics*, 143(13):134701, 2015.

[24] Asghar Aryanfar, Daniel J Brooks, AgustÃn J Colussi, Boris V Merinov, William A Goddard III, and Michael R Hoffmann. Thermal relaxation of lithium dendrites. *Phys. Chem. Chem. Phys.*, 17(12):8000–8005, 2015.

[25] Corey T Love, Olga A Baturina, and Karen E Swider-Lyons. Observation of lithium dendrites at ambient temperature and below. *ECS Electrochemistry Letters*, 4(2):A24, 2015.

[26] Yuanzhou Yao, Xiaohui Zhao, Amir A Razzaq, Yuting Gu, Xietao Yuan, Rahim Shah, Yuebin Lian, Jinxuan Lei, Qiaoqiao Mu, and Yong Ma. Mosaic rgo layer on lithium metal anodes for effective mediation of lithium plating and stripping. *Journal of Materials Chemistry A*, 2019.

[27] Ji Qian, Yu Li, Menglu Zhang, Rui Luo, Fujie Wang, Yusheng Ye, Yi Xing, Wanlong Li, Wenjie Qu, and Lili Wang. Protecting lithium/sodium metal anode with metal-organic framework based compact and robust shield. *Nano Energy*, 2019.

[28] Wei Deng, Wenhua Zhu, Xufeng Zhou, Fei Zhao, and Zhaoping Liu. Regulating capillary pressure to achieve ultralow areal mass loading metallic lithium anodes. *Energy Storage Materials*, 2019.

[29] Jun Li, Edward Murphy, Jack Winnick, and Paul A Kohl. The effects of pulse charging on cycling characteristics of commercial lithium-ion batteries. *J. Power Sources*, 102(1):302–309, 2001.

[30] S Chandrashekar, Onyekachi Oparaji, Guang Yang, and Daniel Hallinan. Communication 7li mri unveils concentration dependent diffusion in polymer electrolyte batteries. *Journal of The Electrochemical Society*, 163(14):A2988–A2990, 2016.

[31] Asghar Aryanfar, Daniel J Brooks, and William A Goddard. Theoretical pulse charge for the optimal inhibition of growing dendrites. *MRS Advances*, 3(22):1201–1207, 2018.

[32] Alexander W Abboud, Eric J Dufek, and Boryann Liaw. Implications of local current density variations on lithium plating affected by cathode particle size. *Journal of The Electrochemical Society*, 166(4):A667–A669, 2019.

[33] Yaoyu Ren, Yang Shen, Yuanhua Lin, and Ce-Wen Nan. Direct observation of lithium dendrites inside garnet-type lithium-ion solid electrolyte. *Electrochemistry Communications*, 57:27–30, 2015.

[34] Christoffer P Nielsen and Henrik Bruus. Morphological instability during steady electrodeposition at overlimiting currents. *Physical Review E*, 92(5):052310, 2015.

[35] PP Natsiavas, K Weinberg, D Rosato, and M Ortiz. Effect of prestress on the stability of electrode–electrolyte interfaces during charging in lithium batteries. *Journal of the Mechanics and Physics of Solids*, 95:92–111, 2016.

[36] N. Schweikert, A. Hofmann, M. Schulz, M. Scheuermann, S. T. Boles, T. Hanemann, H. Hahn, and S. Indris. Suppressed lithium dendrite growth in lithium batteries using ionic liquid electrolytes: Investigation by electrochemical impedance spectroscopy, scanning electron microscopy, and in situ li-7 nuclear magnetic resonance spectroscopy. *J. Power Sources*, 228:237–243, 2013.

[37] Reza Younesi, Gabriel M Veith, Patrik Johansson, Kristina EdstrÃ¶m, and Tejs Vegge. Lithium salts for advanced lithium batteries: Li-metal, li-o 2, and li-s. *Energy and Environmental Science*, 8(7):1905–1922, 2015.

[38] Soon-Ki Jeong, Hee-Young Seo, Dong-Hak Kim, Hyun-Kak Han, Jin-Gul Kim, Yoon Bae Lee, Yasutoshi Iriyama, Takeshi Abe, and Zempachi Ogumi. Suppression of dendritic lithium formation by using concentrated electrolyte solutions. *Electrochemistry communications*, 10(4):635–638, 2008.

[39] Chen Xu, Zeeshan Ahmad, Asghar Aryanfar, Venkatasubramanian Viswanathan, and Julia R Greer. Enhanced strength and temperature dependence of mechanical properties of li at small scales and its implications for li metal anodes. *Proceedings of the National Academy of Sciences*, 114(1):57–61, 2017.

[40] Guangyu Liu, Dandan Wang, Jianyu Zhang, Andrew Kim, and Wei Lu. Preventing dendrite growth by a soft piezoelectric material. *ACS Materials Letters*, 1(5):498–505, 2019.

[41] Rangeet Bhattacharyya, Baris Key, Hailong Chen, Adam S Best, Anthony F Hollenkamp, and Clare P Grey. In situ nmr observation of the formation of metallic lithium microstructures in lithium batteries. *Nat. Mater.*, 9(6):504, 2010.

[42] S Chandrashekar, Nicole M Trease, Hee Jung Chang, Lin-Shu Du, Clare P Grey, and Alexej Jerschow. 7li mri of li batteries reveals location of microstructural lithium. *Nat. Mater.*, 11(4):311–315, 2012.

[43] Yunsong Li and Yue Qi. Energy landscape of the charge transfer reaction at the complex li/sei/electrolyte interface. *Energy & Environmental Science*, 2019.

[44] Laleh Majari Kasmaee, Asghar Aryanfar, Zarui Chikneyan, Michael R Hoffmann, and Agustin J Colussi. Lithium batteries: Improving solid-electrolyte interphases via underpotential solvent electropolymerization. *Chem. Phys. Lett.*, 661:65–69, 2016.

[45] J. N. Chazalviel. Electrochemical aspects of the generation of ramified metallic electrodeposits. *Phys. Rev. A*, 42(12):7355–7367, 1990.

[46] C. Monroe and J. Newman. Dendrite growth in lithium/polymer systems - a propagation model for liquid electrolytes under galvanostatic conditions. *J. Electrochem. Soc.*, 150(10):A1377–A1384, 2003.

[47] Thomas A Witten and Leonard M Sander. Diffusion-limited aggregation. *Phys. Rev. B*, 27(9):5686, 1983.

[48] Xin Zhang, Q Jane Wang, Katharine L Harrison, Katherine Jungjohann, Brad L Boyce, Scott A Roberts, Peter M Attia, and Stephen J Harris. Rethinking how external pressure can suppress dendrites in lithium metal batteries. *Journal of The Electrochemical Society*, 166(15):A3639–A3652, 2019.

[49] V. Fleury. Branched fractal patterns in non-equilibrium electrochemical deposition from oscillatory nucleation and growth. *Nature*, 390(6656):145–148, 1997.

[50] Asghar Aryanfar, Daniel Brooks, Boris V. Merinov, William A. Goddard Iii, AgustÃn J. Colussi, and Michael R. Hoffmann. Dynamics of lithium dendrite growth and inhibition: Pulse charging experiments and monte carlo calculations. *The Journal of Physical Chemistry Letters*, 5(10):1721–1726, 2014.

[51] Asghar Aryanfar, Michael R Hoffmann, and William A Goddard III. Finite-pulse waves for efficient suppression of evolving mesoscale dendrites in rechargeable batteries. *Physical Review E*, 100(4):042801, 2019.

[52] Wenyu Mu, Xunliang Liu, Zhi Wen, and Lin Liu. Numerical simulation of the factors affecting the growth of lithium dendrites. *Journal of Energy Storage*, 26:100921, 2019.

[53] David R Ely, Aniruddha Jana, and R Edwin GarcÃa. Phase field kinetics of lithium electrodeposits. *J. Power Sources*, 272:581–594, 2014.

[54] Daniel A Cogswell. Quantitative phase-field modeling of dendritic electrodeposition. *Physical Review E*, 92(1):011301, 2015.

[55] Rohan Akolkar. Mathematical model of the dendritic growth during lithium electrodeposition. *J. Power Sources*, 232:23–28, 2013.

[56] F. Orsini A.D. Pasquier B. Beaudoin J.M. Tarascon. In situ scanning electron microscopy (sem) observation of interfaces with plastic lithium batteries. *J. Power Sources*, 76:19–29, 1998.

[57] Richard G. Budynas, J. Keith Nisbett, and Joseph Edward Shigley. *Shigley's Mechanical Engineering Design*. McGraw-Hill, 2016.

[58] Stephen P Timoshenko and James M Gere. *Theory of elastic stability*. Courier Corporation, 2009.

[59] Murari Lal Gambhir. *Stability analysis and design of structures*. Springer Science & Business Media, 2004.

[60] William D Callister Jr and David G Rethwisch. *Callister's materials science and engineering*. John Wiley and Sons, 2020.

[61] Julia R Greer, Warren C Oliver, and William D Nix. Size dependence of mechanical properties of gold at the micron scale in the absence of strain gradients. *Acta Materialia*, 53(6):1821–1830, 2005.

[62] Julia R Greer and Jeff Th M De Hosson. Plasticity in small-sized metallic systems: Intrinsic versus extrinsic size effect. *Progress in Materials Science*, 56(6):654–724, 2011.